Inducing and Manipulating Heteroelectronic States in a Single MoS_2 Thin Flake

Q. H. Chen,[2] J. M. Lu,[1] L. Liang,[1] O. Zheliuk,[1] A. Ali,[1] P. Sheng,[2] and J. T. Ye[1,*]
[1]Device Physics of Complex Materials, Zernike Institute for Advanced Materials, Nijenborgh 4, 9747 AG Groningen, Netherlands
[2]Department of Physics, Hong Kong University of Science and Technology, Clear Water Bay, Hong Kong, China
(Received 10 April 2017; revised manuscript received 26 June 2017; published 5 October 2017)

By dual gating a few-layer MoS_2 flake, we induce spatially separated electronic states showing superconductivity and Shubnikov–de Haas (SdH) oscillations. While the highly confined superconductivity forms at the K/K' valleys of the topmost layer, the SdH oscillations are contributed by the electrons residing in the Q/Q' valleys of the rest of the bottom layers, which is confirmed by the extracted Landau level degeneracy of 3, electron effective mass of $0.6m_e$, and carrier density of 5×10^{12} cm^{-2}. Mimicking conventional heterostructures, the interaction between the heteroelectronic states can be electrically manipulated, which enables "bipolarlike" superconducting transistor operation. The off-on-off switching pattern can be continuously accessed at low temperatures by a field effect depletion of carriers with a negative back gate bias and the proximity effect between the top superconducting layer and the bottom metallic layers that quenches the superconductivity at a positive back gate bias.

DOI: 10.1103/PhysRevLett.119.147002

Traditional heterojunctions are constructed by growing semiconducting films with dissimilar electronic structures on top of each other. Recently, a new class of heterostructures has been developed by stacking different two-dimensional (2D) atomic crystals with the van der Waals (vdW) force [1–3]. Strong in-plane covalent bonding prevents the interdiffusion of atoms; hence, the stacking is not restricted by a lattice parameter mismatch. Many novel electronic functionalities have been developed through various combinations of atomically thin 2D crystals [4–13]. In the study of vdW heterostructures, transition metal dichalcogenides (TMDs) with the formula MX_2 (M, Mo, W, Ta, Nb, etc., X, S, Se, or Te) are of particular interest because of their diverse electronic properties. Because of their structural similarity, TMDs have a quite unified band structure with the Fermi level located at different heights, depending on the number of valence electrons of the metal element [14]. Correspondingly, TMDs show electronic properties ranging from semiconducting [15,16] to metallic [17] and even superconducting [18,19]. Theoretically, the Fermi level of one TMD can be shifted by a field effect to access the electronic properties of other TMDs; therefore, the functionalities of vdW heterostructures can be realized in a single TMD material by inducing heteroelectronic states in different layers. However, traditional solid state gates are generally too weak to achieve this goal. Thanks to the recently developed ionic liquid gating technique [20–29], the Fermi level can be shifted in a much larger amount and exotic electronic properties appear; e.g., superconductivity with Ising protection has been observed in ionic gated MoS_2 [21,22,28,29].

In this study, by combining the advantages of an ionic liquid top gate and a solid state back gate, we show that the electronic states of the top and bottom surfaces of a few-layer MoS_2 flake can be independently controlled, resembling the process of stacking a conventional vdW heterostructure. In a five-layer device, both superconductivity and pronounced Shubnikov–de Haas (SdH) oscillations are observed. Robust Ising protection suggests that the superconducting state forms at the K/K' valleys of the topmost layer, while the SdH oscillations are contributed by the electrons residing in the Q/Q' valleys of the bottom layers. Moreover, by employing a high-κ dielectric back gate, we induce an interaction between the top superconducting layer and the bottom layers, manifesting as the proximity effect that weakens the superconductivity.

Figure 1(a) shows schematically the heteroelectronic states formed in a dual-gate MoS_2 transistor. Superconductivity can be routinely induced by ionic gating when the carrier density (n_{2D}) reaches $\sim 10^{14}$ cm^{-2} (Supplemental Material Figs. S1 and S2 [30]). Theoretical calculations show that the carrier distribution in individual layers decays exponentially from the top to the bottom due to a strong Thomas-Fermi screening effect [40,41]; i.e., n_{2D} of the second layer contains only 10% of the total induced carrier in contrast with nearly 90% being accumulated on the topmost one. The topmost layer becomes electronically isolated and behaves like a monolayer. Superconductivity exists only in the topmost layer, since n_{2D} of the second layer is $\sim 10^{13}$ cm^{-2}, which is far below the critical value for reaching superconductivity [21,22].

According to the *ab initio* calculation of the density of states (DOS) [21], the Fermi energy E_F is shifted by $\sim$0.2 eV from the conduction band edge corresponding to a doping level of n_{2D} $\sim 10^{14}$ cm^{-2}. Because of the inversion symmetry breaking caused by the field effect, calculations [42] show that the band structure of a gated multilayer mimics that of a monolayer, where the doping fills the band edge at the K/K' valleys. With very strong gating, E_F may cross the bottom of the Q/Q' valleys [in the midway between the Γ and K/K' points, Fig. 1(b)]. Nevertheless, the observed 2D behavior and large in-plane critical field

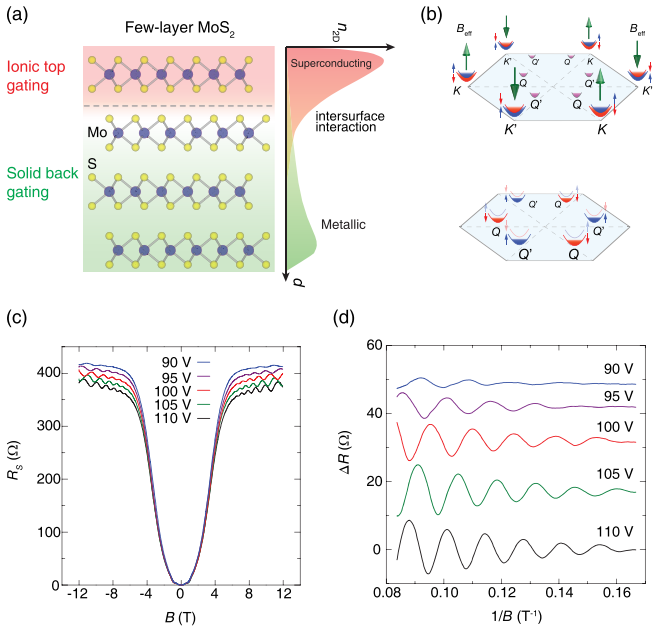

FIG. 1. (a) Schematic illustration of the structure of few-layer MoS_2 and carrier distribution induced by an ionic gate (red) and a back gate (green). (b) Simplified band diagram for the top and bottom electronic states. Different colors represent different spin bands [spin up (down), blue (red)]. Large arrows indicate the intrinsic effective Zeeman field originated from spin-orbit coupling. (c) Magnetoresistance of a dual-gate MoS_2 transistor on an h-BN substrate, measured at $T = 2$ K for $V_{BG} = 90$, 95, 100, 105, and 110 V. (d) SdH oscillations as a function of $1/B$ after subtracting the magnetoresistance background. The curves are vertically shifted for clarity.

(B_{c2}) (Supplemental Material Fig. S2 [30]) suggest that the superconductivity is predominantly contributed by the electrons residing in the K/K' valleys [22,29]. Strong spin orbital coupling and inversion symmetry breaking (by ionic gating) induce a Zeeman-like effective magnetic field B_{eff} (~100 T), oppositely applied at the K/K' points [Fig. 1(b)]. Spins of electrons in the Cooper pairs are polarized to the out-of-plane direction by this Zeeman field, which protects their orientation from being realigned by in-plane magnetic fields, leading to a large in-plane B_{c2} (Ising protection). The spin orbital splitting gap (~6.2 meV) obtained from the experiment is comparable to the value expected from theoretical calculations at the K/K' points (~3 meV) [43].

On the other hand, the back gate accumulates a smaller amount of carriers compared with ionic gating, but the induced carriers preferentially couple to the layers at the bottom surface because of the geometric configuration [44]. Neglecting the quasi-isolated topmost layer, the minima of the conduction band for the bottom layers resume to the Q/Q' valleys. Considering the low carrier density induced by the back gate, the Fermi energy is a few meV above the conduction band edge; thus, the induced electrons primarily occupy the Q/Q' valleys of the bottom layers [Fig. 1(b)].

Figure 1(c) shows the longitudinal magnetoresistance of a five-layer MoS_2 device on a substrate composed of h-BN/SiO_2 (30/300 nm), at different back gate voltages (V_{BG}). While a zero resistance state is observed at zero magnetic field B, pronounced SdH oscillations appear at high fields where superconductivity is suppressed. After subtracting the magnetoresistance background [Fig. 1(d)], SdH oscillations can be clearly observed as a periodic function of $1/B$, and the oscillation frequency decreases with increasing V_{BG}. The envelope function of the SdH oscillations can be well described by the Lifshitz-Kosevich formula [45,46]

$$\Delta R = 4R_0 e^{-\alpha T_D} \alpha T / \sinh(\alpha T), \tag{1}$$

where $\alpha = 2\pi^2 k_B/\hbar\omega_c$, R_0 is the resistance at zero field, $\omega_c = eB/m^*$ the cyclotron frequency, and m^* the effective mass of electrons. $T_D = \hbar/2\pi k_B\tau$ is the Dingle temperature, with τ being the scattering time. n_{2D} is related to the period of oscillation through $n_{2D} = geB_F/h$, where B_F is the oscillation frequency in $1/B$, $g = g_s g_v$ is the Landau level degeneracy, and g_s and g_v the spin and valley degeneracy, respectively. On the other hand, the oscillation is apparently modulated by the back gate, so a change of n_{2D} can be deduced from the back gate voltage and capacitance through $n_{2D} = C_g(V_{BG} - V_{th})/e$, where $C_g = 10.5$ nF/cm^2 is the capacitance per unit area for 300 nm SiO_2 and 30 nm h-BN used in this device. Therefore, $B_F = (hC_g/ge^2)(V_{BG} - V_{th})$. From the linear fitting in Fig. 2(a), we obtain the Landau level degeneracy $g = 3.16$, which agrees with previous reports [47,48]. Because of the inversion symmetry broken by the out-of-plane electrical field of ionic gating, the energy bands at the Q/Q' valleys split into two subbands for different spin polarizations. At zero magnetic field, the lower subbands at $3Q$ and $3Q'$ valleys share the same energy, so the degeneracy is 6 [Fig. 1(b)]. At high magnetic fields, the degeneracy between Q and Q' valleys is lifted by the spin and valley Zeeman splitting [49–51]. As a result, only $3Q$ (or $3Q'$) valleys are occupied [inset in Fig. 2(a)], leading to a degeneracy of 3, which is highly consistent with our observation value of 3.16.

With the obtained Landau level degeneracy, the carrier density for the SdH oscillations can be calculated from $n_{2D} = geB_F/h$ as shown in Fig. 2(b) (dark green dots and dashed line). For comparison, the red shaded area in Fig. 2(b) indicates the carrier density for achieving superconductivity referring to the phase diagram [21]. The carrier densities calculated from the SdH oscillations (~5×10^{12} cm^{-2}) are more than one order of magnitude lower than what is required for the onset of superconductivity (~6×10^{13} cm^{-2}), suggesting the presence of two types of carriers with different densities. This is also supported by the Hall resistance, which exhibits a nonlinear behavior that can be well fitted by a two-band model (Supplemental Material Fig. S6 [30]). Similar behavior was observed at the $LaTiO_3/SrTiO_3$ interface [52], where the back gate induced high-mobility electrons that were spatially separated from the low-mobility superconducting electron gas. Therefore,

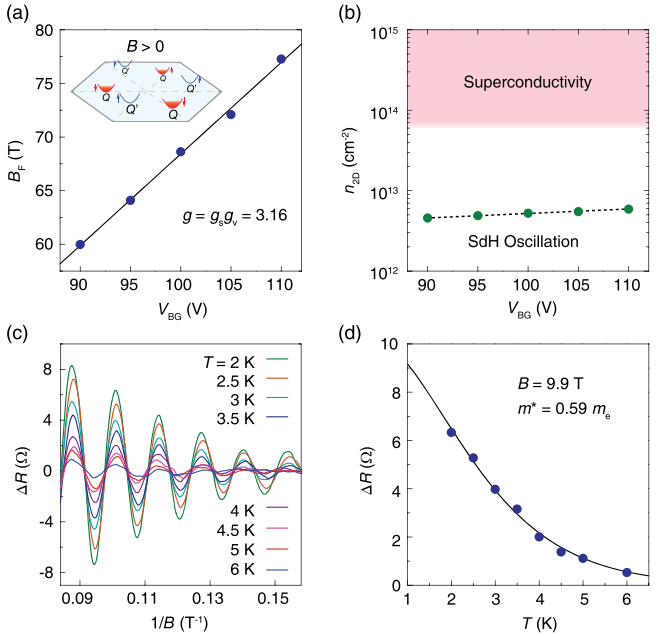

FIG. 2. (a) Oscillation frequency B_F as a function of V_{BG}. The solid line indicates the best linear fitting, yielding a degeneracy of 3.16. Inset: Illustration of the energy bands under a magnetic field, where the degeneracy of Q and Q' valleys is lifted. (b) Calculated carrier density from the SdH oscillations as a function of V_{BG} (dark green dots and dashed guiding line). The red shaded area indicates the carrier density for the superconducting phase. (c) SdH oscillations as a function of the temperature from 2 to 6 K, with $V_{\mathrm{BG}}=110\,\mathrm{V}$. (d) Temperature dependence of the oscillation amplitude at $B = 9.9$ T, giving an electron effective mass of $0.59m_e$.

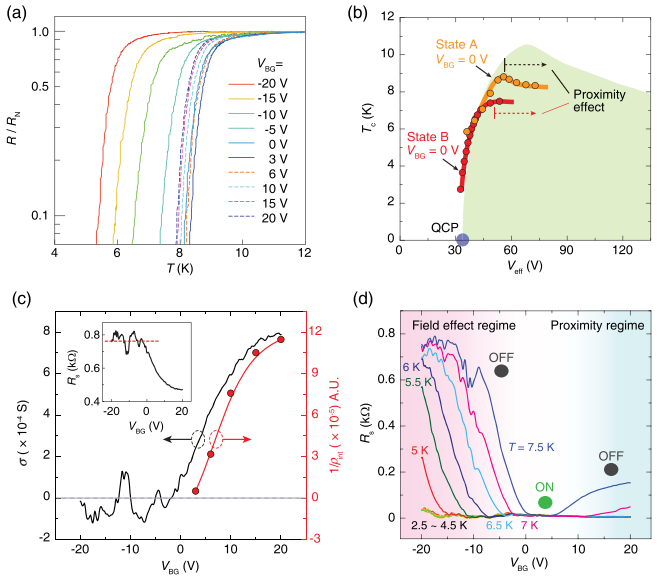

FIG. 3. (a) Temperature dependence of the sheet resistance R_s, normalized by the normal resistance at 13 K. (b) Change of T_c as a function of V_{BG}; the solid lines are guidance for the eyes. State A (orange) is extracted from panel (a); state B (red) corresponds to a different ionic gating state of the same device. The shaded area represents the phase diagram from Ref. [21]. (c) Extracted conductivity of the bottom layers (black solid curve, left axis) and calculated $1/\rho_{\mathrm{int}}$ (red dots connected by the solid guideline, right axis) as a function of V_{BG}. Inset: V_{BG} dependence of R_s at 13 K. (d) R_s as a function of V_{BG} at different temperatures, showing continuous "bipolar" switching of superconductivity. The off and on refer to finite and zero resistances, respectively.

the deviation from the linear Hall effect serves as clear evidence for the existence of heteroelectronic states in different layers: high-density electron in the topmost layer for superconductivity and low-density electrons in the bottom layers for SdH oscillations, respectively.

Theoretical calculations [53] show that the electron effective mass is $0.5m_e$ in the K/K' valleys and $0.6m_e$ in the Q/Q' valleys. By fitting the temperature dependence of the oscillation amplitude with the Lifshitz-Kosevich formula [Figs. 2(c) and 2(d)], the effective mass of electrons participating in the SdH oscillations can be determined as $m^* = 0.59m_e$ (m_e is the electron rest mass), which is highly consistent with the electrons residing in the Q/Q' valleys. Overall, the SdH oscillations can be unambiguously attributed to the Q/Q' valleys of the bottom layers, while the superconductivity is predominantly contributed by the K/K' valleys of the topmost layer.

As the first step, inducing two independent electronic states of dissimilar properties achieves only the structural similarity of vdW heterostructures. More importantly, an interaction between the heteroelectronic states can emerge when their wave functions overlap, as shown in the right panel in Fig. 1(a). To implement this idea, we fabricated a four-layer MoS_2 device on a HfO_2 (50 nm) substrate. The high-κ dielectric allows continuous tuning of the carrier density within $\Delta n_{2D} \sim \pm 3 \times 10^{13}$ cm^{-2} by biasing up to ± 20 V. Figure 3(a) shows the temperature dependence of the normalized sheet resistance for a superconducting state with $T_c = 8.5$ K at $V_{\mathrm{BG}} = 0$ V. The T_c [orange dots in Fig. 3(b), defined as 50% of the normal resistance] increases monotonically from -20 to 3 V but surprisingly starts to decrease at $V_{\mathrm{BG}} > 3\,\mathrm{V}$, deviating from the established phase diagram [21]. Similar behavior is observed in a different superconducting state (smaller ionic gate voltage) with $T_c = 3.5$ K at $V_{\mathrm{BG}} = 0$ V [red dots in Fig. 3(b)], although the deviation initiates at a higher V_{BG}. In Fig. 3(b), the horizontal axis is converted to an effective gate voltage V_{eff} (calculated by the back gate capacitance) so that we can directly compare the back gate dependence of T_c with the phase diagram. For $V_{\mathrm{BG}} < V_{\mathrm{th}}$ (threshold voltage of the bottom layers, $\approx$0 V; see Supplemental Material Fig. S1 [30]), the bottom layers remains insulating and acts as an additional dielectric layer for back gate tuning of the carrier density in the topmost layer; therefore, T_c decreases in accordance with the phase diagram. For $V_{\mathrm{BG}} > V_{\mathrm{th}}$, however, the bottom layers become metallic and screen out V_{BG}. The back gate cannot effectively accumulate carriers in the topmost layer; therefore, T_c is not expected to change.

The observed reduction of T_c could be caused by the proximity effect, because Cooper pairs of the topmost layer

can diffuse into the bottom layers if they become metallic. Similar to a conventional superconductor-normal metal (SN) bilayer structure [54–57], the T_c of a superconducting thin film decreases on a metallic substrate due to the proximity effect. Following the Usadel equation [58], Fominov and Feigel'man developed the following relation to describe the influence of a metallic substrate on the superconducting properties [54]:

$$\ln\frac{T_{cs}}{T_c}=\frac{\tau_N}{\tau_S+\tau_N}\left[\psi\left(\frac{1}{2}+\frac{h(\tau_S+\tau_N)}{2\pi k_B T_c\tau_S\tau_N}\right)-\psi\left(\frac{1}{2}\right)-\ln\sqrt{1+\left(\frac{\tau_S+\tau_N}{\tau_S\tau_N\omega_D}\right)^2}\right], \quad (2)$$

where $\psi(x)$ is the digamma function, T_{cs} the original transition temperature, and T_c the transition temperature on a metallic substrate. τ_N and τ_S are given by $\tau_N = 2\pi(V_N d_N/V_S^2)\rho_{\rm int}$ and $\tau_S = 2\pi(d_S/V_S)\rho_{\rm int}$, respectively, and V_N and V_S are the Fermi velocities of the normal and superconducting states, respectively; d_S and d_N are the thickness of the superconducting and normal layers, respectively. $\rho_{\rm int}$ is defined as the dimensionless resistance between the SN layers, parameterizing the coupling strength. $\rho_{\rm int}$ decreases as the coupling between the SN layers increases. The logarithmic term in Eq. (2) is important only for a perfect interface ($\rho_{\rm int}\to 0$), which can be omitted in the present analysis, because the interface between the top and bottom channels is far from being perfect (large $\rho_{\rm int}$).

At $V_{\rm BG}=3$ V, just before switching on the bottom layers, we obtained $T_c = T_{cs} = 8.75$ K. With the increase of $V_{\rm BG}$ and decrease of T_c, the coupling parameter in Eq. (2) can be numerically solved. In Fig. 3(c), we plot $1/\rho_{\rm int}$ as the analogy of the dimensionless interface conductivity. The obtained small interface conductivity corroborates the omission of the logarithmic term in Eq. (2). For comparison, we extract the conductivity of the bottom layers by assuming that the $V_{\rm BG}$ dependence of R_s [inset in Fig. 3(c)] is contributed by the two parallel conducting channels as $(1/R_S) = (1/R_{\rm top}) + (1/R_{\rm bottom})$. When the bottom channel is in the off state ($R_{\rm bottom}\to\infty$) at $V_{\rm BG} < V_{\rm th}$, we estimate that $R_{\rm top}\approx 750\ \Omega$, which saturates at negative $V_{\rm BG}$. The extracted conductivity of the bottom channel is shown in Fig. 3(c) (black curve), where we can see a clear correlation between the conductivity of the bottom layers and the interface conductivity $1/\rho_{\rm int}$. This close correlation strongly suggests that the formation of a metallic bottom state suppresses the superconductivity in the topmost layer through the proximity effect.

Based on this gate viable coupling, a "bipolarlike" superconducting transistor operation can be established as shown in Fig. 3(d), where the on and off states refer to zero and finite resistance, respectively. At a relatively high temperature ($T = 7.5$ K), the superconducting state can be switched off by both positive and negative back gate voltages with different working principles: (i) for $V_{\rm BG} < 0$ V, the bottom channel remains insulating and acts like an additional dielectric layer for the field effect tuning of the superconductivity in the topmost layer; (ii) for $V_{\rm BG} > 0$ V, the bottom channel becomes metallic, which leads to a proximity effect that weakens the superconductivity. Well below T_c (for $T < 5$ K) where the superconducting pairing is strong, both the field effect and proximity effect show little effect.

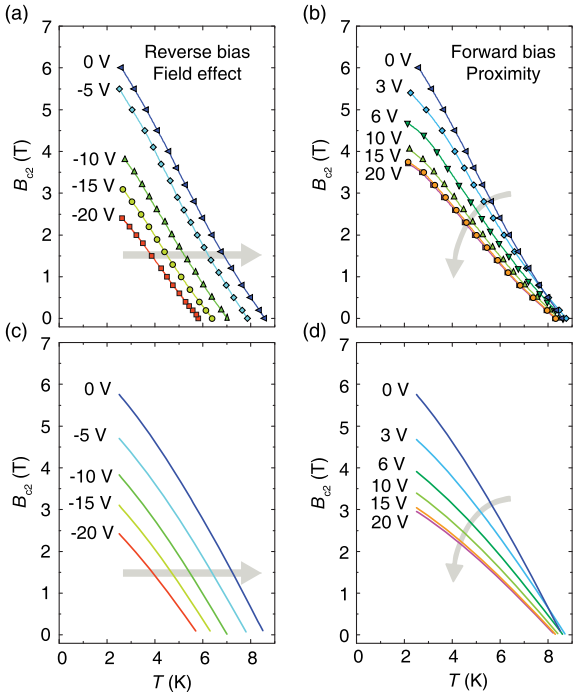

FIG. 4. Temperature dependence of B_{c2} for different $V_{\rm BG}$ from (a) −20 to 0 V and (b) 0 to 20 V. (c),(d) The calculated temperature dependence of B_{c2} corresponding to the same regimes shown in panels (a) and (b). The left and right panels correspond to the field effect regime and the proximity effect regime, respectively.

The interaction between the heteroelectronic states also significantly affects other physical parameters associated with the superconductivity. The upper critical field B_{c2} (defined as 50% of the normal state resistance) varies drastically due to the formation of a metallic bottom state. As shown in Fig. 4, the B_{c2} ($B\perp ab$ plane) is compared in two regimes: the field effect regime ($V_{\rm BG} < 0$ V) and the proximity effect regime ($V_{\rm BG} > 0$ V). At $V_{\rm BG} < 0$ V, the temperature dependences of B_{c2} at different $V_{\rm BG}$ display as a series of nearly parallel lines, indicating that the decrease of B_{c2} is proportional to the decrease of T_c. At $V_{\rm BG} > 0$ V, however, the slope of the $B_{c2} - T_c$ curve decreases substantially in contrast to the small change of T_c. To further investigate this unusual behavior, we calculated the temperature dependence of B_{c2} as shown in Figs. 4(c) and 4(d) (more details are discussed in Supplemental Material Sec. VI [30]). The result reproduces all the experimental features: the left and right panels are

characterized as the V_{BG} control of the field effect depletion and proximity effect, respectively. The underlying physical mechanism can be phenomenologically explained by the Werthamer-Helfand-Hohenberg theory [59], which describes the temperature and mean free path dependence of the B_{c2} of type-II superconductors. The slope of B_{c2} at T_c, $(dB_{c2}/dT)_{T=T_c}$, is inversely proportional to the electron mean free path. In our device at large positive V_{BG}, the bottom channel becomes more metallic and acts as an effective screening layer, which reduces the charged impurity scatterings in the topmost layer. Consequently, the mean free path of the electron increases significantly, leading to the suppression of B_{c2}.

In summary, we induced heteroelectronic states in a single MoS_2 thin flake, in which both superconductivity and SdH oscillations are observed. By controlling the coupling strength between the top and bottom states, we created a bipolarlike superconducting transistor. A metallic bottom state significantly suppress the upper critical field, implying that the interlayer coupling played an important role in determining the electronic properties of the artificial heterostructure. The manipulation of heteroelectronic states in a single vdW material provides a new degree of freedom in electronic band structure engineering and is promising for developing a unique family of homojunctions, whose electronic and optical properties will largely enrich the functionalities of vdW structures.

We thank J. Harkema for technical support. Q. H. C. thanks the scholarship from The Ubbo Emmius Fund. J. T. Y. and Q. H. C. thank the stichting voor Fundamenteel Onderzoek der Materie (FOM, FV157) and FlagERA iSpinText for financial support. J. T. Y. acknowledges funding from the European Research Council (consolidator Grant No. 648855, Ig-QPD). P. S. thanks the support from the Research Grants Council of Hong Kong SAR Government (Grant No. 16304314/HKUST).

*Corresponding author.
j.ye@rug.nl

[1] K. S. Novoselov, D. Jiang, F. Schedin, T. J. Booth, V. V. Khotkevich, S. V. Morozov, and A. K. Geim, Proc. Natl. Acad. Sci. U.S.A. **102**, 10451 (2005).
[2] K. S. Novoselov, A. Mishchenko, A. Carvalho, and A. H. C. Neto, Science **353**, aac9439 (2016).
[3] A. K. Geim and I. V. Grigorieva, Nature (London) **499**, 419 (2013).
[4] T. Georgiou, R. Jalil, B. D. Belle, L. Britnell, R. V. Gorbachev, S. V. Morozov, Y.-J. Kim, A. Gholinia, S. J. Haigh, O. Makarovsky, L. Eaves, L. A. Ponomarenko, A. K. Geim, K. S. Novoselov, and A. Mishchenko, Nat. Nanotechnol. **8**, 100 (2013).
[5] B. Hunt, J. D. Sanchez-Yamagishi, A. F. Young, M. Yankowitz, B. J. LeRoy, K. Watanabe, T. Taniguchi, P. Moon, M. Koshino, P. Jarillo-Herrero, and R. C. Ashoori, Science **340**, 1427 (2013).
[6] H. Fang, C. Battaglia, C. Carraro, S. Nemsak, B. Ozdol, J. S. Kang, H. A. Bechtel, S. B. Desai, F. Kronast, A. A. Unal, G. Conti, C. Conlon, G. K. Palsson, M. C. Martin, A. M. Minor, C. S. Fadley, E. Yablonovitch, R. Maboudian, and A. Javey, Proc. Natl. Acad. Sci. U.S.A. **111**, 6198 (2014).
[7] Z. Wang, D.-K. Ki, H. Chen, H. Berger, A. H. MacDonald, and A. F. Morpurgo, Nat. Commun. **6**, 8339 (2015).
[8] J. Kang, J. Li, S.-S. Li, J.-B. Xia, and L.-W. Wang, Nano Lett. **13**, 5485 (2013).
[9] F. Withers, O. Del Pozo-Zamudio, A. Mishchenko, A. P. Rooney, A. Gholinia, K. Watanabe, T. Taniguchi, S. J. Haigh, A. K. Geim, A. I. Tartakovskii, and K. S. Novoselov, Nat. Mater. **14**, 301 (2015).
[10] C.-H. Lee, G.-H. Lee, A. M. van der Zande, W. Chen, Y. Li, M. Han, X. Cui, G. Arefe, C. Nuckolls, T. F. Heinz, J. Guo, J. Hone, and P. Kim, Nat. Nanotechnol. **9**, 676 (2014).
[11] G. W. Shim, K. Yoo, S.-B. Seo, J. Shin, D. Y. Jung, I.-S. Kang, C. W. Ahn, B. J. Cho, and S.-Y. Choi, ACS Nano **8**, 6655 (2014).
[12] W. Zhang, Q. Wang, Y. Chen, Z. Wang, and A. T. S. Wee, 2D Mater. **3**, 022001 (2016).
[13] Q. H. Wang, K. Kalantar-Zadeh, A. Kis, J. N. Coleman, and M. S. Strano, Nat. Nanotechnol. **7**, 699 (2012).
[14] L. F. Mattheiss, Phys. Rev. B **8**, 3719 (1973).
[15] K. F. Mak, C. Lee, J. Hone, J. Shan, and T. F. Heinz, Phys. Rev. Lett. **105**, 136805 (2010).
[16] B. Radisavljevic and A. Kis, Nat. Mater. **12**, 815 (2013).
[17] J. A. Wilson, F. J. Di Salvo, and S. Mahajan, Phys. Rev. Lett. **32**, 882 (1974).
[18] X. Xi, Z. Wang, W. Zhao, J.-H. Park, K. T. Law, H. Berger, L. Forró, J. Shan, and K. F. Mak, Nat. Phys. **12**, 139 (2016).
[19] B. Sipos, A. F. Kusmartseva, A. Akrap, H. Berger, L. Forró, and E. Tutiš, Nat. Mater. **7**, 960 (2008).
[20] H. Yuan, H. Shimotani, A. Tsukazaki, A. Ohtomo, M. Kawasaki, and Y. Iwasa, Adv. Funct. Mater. **19**, 1046 (2009).
[21] J. T. Ye, Y. J. Zhang, R. Akashi, M. S. Bahramy, R. Arita, and Y. Iwasa, Science **338**, 1193 (2012).
[22] J. M. Lu, O. Zheliuk, I. Leermakers, N. F. Q. Yuan, U. Zeitler, K. T. Law, and J. T. Ye, Science **350**, 1353 (2015).
[23] W. Shi, J. Ye, Y. Zhang, R. Suzuki, M. Yoshida, J. Miyazaki, N. Inoue, Y. Saito, and Y. Iwasa, Sci. Rep. **5**, 12534 (2015).
[24] K. Ueno, S. Nakamura, H. Shimotani, A. Ohtomo, N. Kimura, T. Nojima, H. Aoki, Y. Iwasa, and M. Kawasaki, Nat. Mater. **7**, 855 (2008).
[25] J. T. Ye, S. Inoue, K. Kobayashi, Y. Kasahara, H. T. Yuan, H. Shimotani, and Y. Iwasa, Nat. Mater. **9**, 125 (2010).
[26] Y. J. Zhang, J. T. Ye, Y. Yomogida, T. Takenobu, and Y. Iwasa, Nano Lett. **13**, 3023 (2013).
[27] S. Jo, D. Costanzo, H. Berger, and A. F. Morpurgo, Nano Lett. **15**, 1197 (2015).
[28] D. Costanzo, S. Jo, H. Berger, and A. F. Morpurgo, Nat. Nanotechnol. **11**, 339 (2016).
[29] Y. Saito, Y. Nakamura, M. S. Bahramy, Y. Kohama, J. Ye, Y. Kasahara, Y. Nakagawa, M. Onga, M. Tokunaga, T. Nojima, Y. Yanase, and Y. Iwasa, Nat. Phys. **12**, 144 (2016).
[30] See Supplemental Material at http://link.aps.org/supplemental/10.1103/PhysRevLett.119.147002 for details on the experimental methods, device characteristics, superconducting properties, scattering time, back gate analysis,

Hall measurement, and calculation of B_{c2}, which includes Refs. [31–39].
[31] K. S. Novoselov, A. K. Geim, S. V. Morozov, D. Jiang, Y. Zhang, S. V. Dubonos, I. V. Grigorieva, and A. A. Firsov, Science **306**, 666 (2004).
[32] P. J. Zomer, M. H. D. Guimarães, J. C. Brant, N. Tombros, and B. J. van Wees, Appl. Phys. Lett. **105**, 013101 (2014).
[33] M. Tinkham, Phys. Rev. **129**, 2413 (1963).
[34] S. Kim, A. Konar, W.-S. Hwang, J. H. Lee, J. Lee, J. Yang, C. Jung, H. Kim, J.-B. Yoo, J.-Y. Choi, Y. W. Jin, S. Y. Lee, D. Jena, W. Choi, and K. Kim, Nat. Commun. **3**, 1011 (2012).
[35] W. Bao, X. Cai, D. Kim, K. Sridhara, and M. S. Fuhrer, Appl. Phys. Lett. **102**, 042104 (2013).
[36] M. Tinkham, *Introduction to Superconductivity*, 2nd ed. (Dover, New York, 2004).
[37] Z. Han, A. Allain, H. Arjmandi-Tash, K. Tikhonov, M. Feigel'man, B. Sacépé, and V. Bouchiat, Nat. Phys. **10**, 380 (2014).
[38] B. Spivak and F. Zhou, Phys. Rev. Lett. **74**, 2800 (1995).
[39] V. M. Galitski and A. I. Larkin, Phys. Rev. Lett. **87**, 087001 (2001).
[40] R. Roldán, E. Cappelluti, and F. Guinea, Phys. Rev. B **88**, 054515 (2013).
[41] N. T. Cuong, M. Otani, and S. Okada, J. Phys. Condens. Matter **26**, 135001 (2014).
[42] T. Brumme, M. Calandra, and F. Mauri, Phys. Rev. B **91**, 155436 (2015).
[43] G.-B. Liu, D. Xiao, Y. Yao, X. Xu, and W. Yao, Chem. Soc. Rev. **44**, 2643 (2015).
[44] S. Das and J. Appenzeller, Nano Lett. **13**, 3396 (2013).
[45] L. M. Lifshitz and A. M. Kosevich, Zh. Eksp. Teor. Fiz. **29**, 730 (1955) Sov. Phys. JETP **2**, 636 (1956).
[46] T. Ando, A. B. Fowler, and F. Stern, Rev. Mod. Phys. **54**, 437 (1982).
[47] Z. Wu, S. Xu, H. Lu, A. Khamoshi, G.-B. Liu, T. Han, Y. Wu, J. Lin, G. Long, Y. He, Y. Cai, Y. Yao, F. Zhang, and N. Wang, Nat. Commun. **7**, 12955 (2016).
[48] X. Cui, G.-H. Lee, Y. D. Kim, G. Arefe, P. Y. Huang, C.-H. Lee, D. A. Chenet, X. Zhang, L. Wang, F. Ye, F. Pizzocchero, B. S. Jessen, K. Watanabe, T. Taniguchi, D. A. Muller, T. Low, P. Kim, and J. Hone, Nat. Nanotechnol. **10**, 534 (2015).
[49] G. Aivazian, Z. Gong, A. M. Jones, R.-L. Chu, J. Yan, D. G. Mandrus, C. Zhang, D. Cobden, W. Yao, and X. Xu, Nat. Phys. **11**, 148 (2015).
[50] Y. Li, J. Ludwig, T. Low, A. Chernikov, X. Cui, G. Arefe, Y. D. Kim, A. M. van der Zande, A. Rigosi, H. M. Hill, S. H. Kim, J. Hone, Z. Li, D. Smirnov, and T. F. Heinz, Phys. Rev. Lett. **113**, 266804 (2014).
[51] A. Srivastava, M. Sidler, A. V. Allain, D. S. Lembke, A. Kis, and A. Imamoğlu, Nat. Phys. **11**, 141 (2015).
[52] J. Biscaras, N. Bergeal, S. Hurand, C. Grossetête, A. Rastogi, R. C. Budhani, D. LeBoeuf, C. Proust, and J. Lesueur, Phys. Rev. Lett. **108**, 247004 (2012).
[53] G.-B. Liu, W.-Y. Shan, Y. Yao, W. Yao, and D. Xiao, Phys. Rev. B **88**, 085433 (2013).
[54] Y. V. Fominov and M. V. Feigel'man, Phys. Rev. B **63**, 094518 (2001).
[55] A. Stępniak, A. Leon Vanegas, M. Caminale, H. Oka, D. Sander, and J. Kirschner, Surf. Interface Anal. **46**, 1262 (2014).
[56] P. G. De Gennes, Rev. Mod. Phys. **36**, 225 (1964).
[57] M. Wolz, C. Debuschewitz, W. Belzig, and E. Scheer, Phys. Rev. B **84**, 104516 (2011).
[58] K. D. Usadel, Phys. Rev. Lett. **25**, 507 (1970).
[59] N. R. Werthamer, E. Helfand, and P. C. Hohenberg, Phys. Rev. **147**, 295 (1966).